In-Situ X-ray Diffraction Analysis of Metastable Austenite Containing Steels Under Mechanical Loading at a Wide Strain Rate Range

MATTI ISAKOV, VEERA LANGI, LALIT PUN, GUILHERME CORRÊA SOARES, INNOKENTY KANTOR, MADS RY VOGEL JØRGENSEN, and MIKKO HOKKA

This paper presents and discusses the methodology and technical aspects of mechanical tests carried out at a wide strain rate range with simultaneous synchrotron X-ray diffraction measurements. The motivation for the study was to develop capabilities for *in-situ* characterization of the loading rate dependency of mechanically induced phase transformations in steels containing metastable austenite. The experiments were carried out at the DanMAX beamline of the MAX IV Laboratory, into which a custom-made tensile loading device was incorporated. The test setup was supplemented with *in-situ* optical imaging of the specimen, which allowed digital image correlation-based deformation analysis. All the measurement channels were synchronized to a common time basis with trigger signals between the devices as well as post-test fine tuning based on diffraction ring shape analysis. This facilitated precise correlation between the mechanical and diffraction data at strain rates up to 1 s^{-1} corresponding to test duration of less than one second. Diffraction data were collected at an acquisition rate of 250 Hz, which provided excellent temporal resolution. The feasibility of the methodology is demonstrated by providing novel data on the kinetics of the martensitic phase transformation in EN 1.4318-alloy following a rapid increase in strain rate (a so-called jump test).

I. INTRODUCTION

THE solid-state phase transformations from the face-centered-cubic (FCC) austenite phase (γ) to a family of (near) body-centered-cubic (BCC) phases (α), such as ferrite, bainite, and martensite, have great importance in steel technology. Of special technological and scientific interest are the mechanically induced martensitic transformations (either stress-assisted or strain-induced), which take place when the parent austenite is externally loaded. These phase transformations offer great potential to improve the mechanical properties of the material by refining the microstructure *during* deformation *via* gradual transformation of the parent austenite to martensite. When the transformation takes place at an optimal rate, a material with excellent ductility and strain hardening properties is achieved. However, the tendency toward the phase transformation is generally known to be very sensitive to the alloy composition and loading conditions, such as temperature and rate of deformation. Moreover, the effects of loading conditions depend on the alloy in question. For example, Enloe *et al.*[1] recently reported a positive strain rate effect in a low-alloy TRIP steel, where metastable austenite is a minor constituent phase. In contrast, in metastable austenitic stainless steels, which are initially nearly fully austenitic and transform readily under quasi-static loading, the phase transformation tendency is notably suppressed as the strain rate is increased (*cf.* Reference 2). These findings exemplify the fact that the mechanical behavior of metastable austenite containing alloys involves a multitude of parallel and cross-linked phenomena, which, despite decades of research and development, are yet to be fully understood.

A major contributor to the above-mentioned challenge is the fact that the means to study microstructural evolution *in-situ* during high strain rate deformation are very limited. Typically, analysis is based on the

MATTI ISAKOV, VEERA LANGI, LALIT PUN, GUILHERME CORRÊA SOARES and MIKKO HOKKA are with the Materials Science and Environmental Engineering, Impact Laboratory, Tampere University, Tampere, Finland. Contact e-mail: matti.isakov@tuni.fi INNOKENTY KANTOR is with the Department of Physics, The Technical University of Denmark, 2880 Lyngby, Denmark and also with the MAX IV Laboratory, Lund University, 224 84 Lund, Sweden. MADS RY VOGEL JØRGENSEN is with Department of Chemistry & iNANO, Aarhus University, 8000 Aarhus C, Denmark and also with the the MAX IV Laboratory, Lund University

metallographic (destructive) sampling of specimens taken from interrupted tests; this method quickly becomes very tedious when sufficient resolution in terms of accumulating deformation is required and carries the challenges related to specimen-to-specimen variation as well as microstructural changes taking place during sample preparation or simply just by the unloading of the material as the test is interrupted (*cf*. Reference 3). Some methods, such as determination of phase fractions based on the changes in the specimen's magnetic properties (*cf*. Reference 4,5) or the use of a metallographic inspection region on the specimen surface (*cf*. References 6, and 7), can be applied to a single specimen. However, the mechanical experiment has to be usually carried out at a low deformation rate or periodically interrupted so that the microstructural data can be collected. In the studies of dynamic deformation properties of materials, this is a major challenge: the interruption of the loading introduces a disturbance in the deformation history, which can affect the material behavior. For example, material temperature increases at high rates of plastic deformation due to the conversion of the external work into heat under the conditions of insufficient heat transfer. If the loading is interrupted, the heat is transferred into the surroundings, which leads to different thermomechanical histories between monotonic and incremental experiments. This is a major challenge for materials with metastable phase structures, especially when taking into account that high rate deformation may involve heterogeneous heating on the microstructural level.[7,8] Similarly, changes in strain rate may affect the evolution of the material dislocation structure (such as the mobile dislocation density), which in turn may influence the phase transformation rate and the mechanical behavior of the material. Therefore, the method used to study the microstructural evolution should disturb these processes as little as possible.

Based on the discussion above, metallurgical development would greatly benefit from a technique that allows phase fraction data to be collected during a high rate mechanical loading experiment without imposing any interruptions on the loading history. Recently, the use of high intensity radiation, either synchrotron X-rays[9–18] or neutrons,[5,19–21] has become a viable option for *in-situ* collection of phase fraction data during mechanical loading. Even though there are practical challenges related to the large resources and infrastructure needed, these methods have the major benefit of producing quantitative crystallographic data from a specimen volume, which is large enough to represent the behavior of the bulk material (thus complementing electron microscopy-based techniques, which produce data from a very limited region of the microstructure). So far, quantitative diffraction analysis of mechanically induced phase transformations has been mainly limited to near static loading, *i.e.*, at strain rates ~ 0.001 s^{-1} or lower. There are reports on synchrotron radiation-based diffraction measurements at very high strain rates (loading duration ~ 1 ms or less), which involve the use of scintillators and high-speed optical cameras.[22–27] However, currently these measurements involve finding a balance between sufficient frame rate and the limitations imposed on the number of frames, signal-to-noise ratio, and resolution of the diffraction data. For example, in a recent study,[28] *in-situ* synchrotron measurements were carried out during very high-frequency cyclic loading by collecting diffraction data over several cycles to ensure high enough signal-to-noise ratio.

Recent developments in the detector technology have opened up possibilities to collect X-ray diffraction data at sampling rates of some hundreds to a few thousand per second *continuously*, *i.e.*, for hundreds or thousands of frames per test. High-Z hybrid pixel detectors offer very low noise levels and efficient detection of hard X-rays, which combined with the very high flux from modern synchrotron beamlines makes time resolved diffraction experiment feasible. As is demonstrated in this paper, this new technology facilitates *in-situ* diffraction measurements at the intermediate (near 1 s^{-1}) strain rate region with excellent temporal resolution. This is a major advance, since now the phase transformation kinetics can be studied in detail over a wide strain rate range extending from quasi-static rates to intermediate strain rates where deformation-induced heating effects are notable.

This paper presents and discusses the methodology used in a recent experimental campaign carried out at the DanMAX beamline of the MAX IV Laboratory 3 GeV synchrotron. The work involved uniaxial tensile tests on metastable austenite containing steel alloys with *in-situ* X-ray diffraction and optical surface strain measurements. The test campaign included tests at a wide strain rate range of 0.001 to 1 s^{-1} (with some trials at 10 s^{-1}) as well as tests with sudden change in strain rate (so-called "jump tests") used to elucidate the strain rate dependency of the phase transformation kinetics. This paper focuses on the methodology side of the tests, while detailed analysis of material behavior will be reported in future publications.

II. *IN-SITU* X-RAY DIFFRACTION MEASUREMENT DURING MECHANICAL LOADING

The main objective of the study was to measure *in-situ* the kinetics of mechanically induced phase transformations taking place at a wide range of strain rates. For this, very good temporal synchronization between the diffraction measurements and mechanical data acquisition signals is required. As explained later, electronical trigger signals were used between the different experimental devices, which already provides adequate synchronization. However, the synchronization can be further improved in post-test analysis by noting that the external load leads to predictable changes in the recorded diffraction rings. That is, analysis of the diffraction ring shape evolution frame-by-frame gives an independent time history of the imposed load, which can be compared with the load record given by the mechanical testing device. The theoretical background of the necessary diffraction analysis is given in the following.

As is well known, the application of monochromatic radiation on a polycrystalline specimen results in the formation of Debye–Scherrer rings on a plane (detector) placed behind the specimen. The angular position (2θ) of these rings is given by the Bragg's law:

$$2d\sin\theta = \lambda, \quad [1]$$

where d is the distance between the diffracting lattice planes and λ is the wavelength of the radiation. The application of external loads on the specimen results in directionally dependent elastic strains, which affect the lattice distances anisotropically and hence the diffraction ring shape. In the experimental conditions used in this study, the only non-zero stress component is the normal stress σ_x. Thus, by utilizing generalized Hooke's law, the elastic strains in the main directions of the specimen can be solved (coordinate system according to Figure 1):

$$\varepsilon_x = \frac{1}{E}\sigma_x, \varepsilon_y = \varepsilon_z = -\frac{v}{E}\sigma_x, \varepsilon_{ij} = 0, \quad [2]$$

where E and v are the Young's modulus and Poisson's ratio of the material, respectively.

The orientation of the diffracting lattice planes is characterized by the azimuthal angle ϕ between the specimen x-direction and the projection of the lattice plane normal on the specimen xy-plane as well as the angle ψ between the lattice plane normal and the specimen z-direction. In the current diffraction experiments, the specimen z-direction and the incident beam direction coincide, hence $\psi = 90° - \theta$. Thus the ring radius in a given direction can be solved by calculating the respective elastic strain ($\varepsilon_{\phi\psi}$)[29]:

$$\varepsilon_{\phi\psi} = \varepsilon_x \sin^2\psi\cos^2\phi + \varepsilon_y\sin^2\psi\sin^2\phi + \varepsilon_z\cos^2\psi \quad [3]$$

$$\frac{d}{d_0} = \frac{\sin\theta_0}{\sin\theta} = (1 + \varepsilon_{\phi\psi})$$
$$= 1 + \frac{\sigma_x}{E}\left[\sin^2\psi\left(\cos^2\phi - v\sin^2\phi\right) - v\cos^2\psi\right], \quad [4]$$

where d_0 represents the unloaded lattice spacing and linear definition of strain has been used. As is evident from Eq. [4], the application of uniaxial loading results in the diffraction rings (characterized by constant ψ-angle and varying ϕ-angle) becoming ellipses with their short axis aligned with the loading direction ($\phi = 0$).

Quite often the elastic strains in a certain azimuthal direction are determined by following the shifts in the diffraction rings along that direction. This is achieved either by using line detectors or by integrating a narrow strip of the recorded azimuthal range. However, the experimental data can be utilized more efficiently by analyzing the full available azimuthal range as in Reference 30. In the current study, this is done by applying the calculation rules of trigonometric functions ($\sin^2\phi + \cos^2\phi = 1$ and $\sin(\psi) = \sin(90° - \theta_0) = \cos\theta_0$) to Eq. [4] and simplifying:
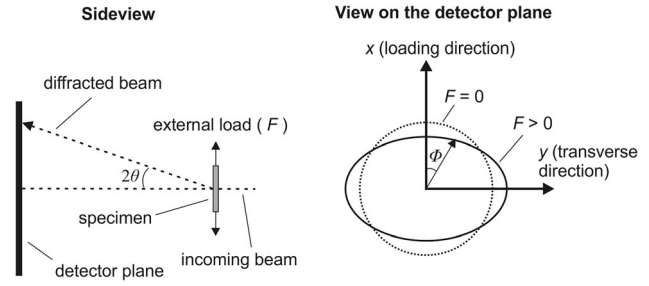

Fig. 1—Schematic description of the *in-situ* diffraction measurement during uniaxial mechanical loading and depiction of the effect of external load on the shape of the diffraction rings.

$$\frac{\sin\theta_0}{\sin\theta} = 1 + \frac{1+v}{E}\sigma_x\cos^2\theta_0\cos^2\phi - \frac{v}{E}\sigma_x \quad [5]$$

According to Eq. [5], the diffraction rings appear as lines in the ($1/\sin\theta$, $\cos^2\phi$)-space, which facilitates straightforward least squares fitting to the data. One coordinate point is of special interest; $\cos^2\phi = 1$, *i.e.*, the ring location in the loading direction, which facilitates the calculation of the elastic strain in the loading direction. It should be noted that the crystalline level elastic parameters (E and v) are anisotropic, *i.e.*, the values are dependent on the family of lattice planes.

III. METHODOLOGY

The experiments were carried out at the DanMAX beamline of the MAX IV Laboratory in Lund, Sweden. Figure 2(a) illustrates the main components of the test setup within the experimental hutch. The diffraction measurements were carried out in transmission geometry with a 35 keV high-energy X-ray beam (wavelength of 0.354 Å and a beam size of 0.5×0.5 mm^2). The diffraction patterns were recorded by a DECTRIS PILATUS3 X 2M CdTe detector (pixel size 172 μm, grid 1679 pixels by 1475 pixels) placed approximately 650 mm behind (downstream) the specimen. The detector is positioned so that the direct beam is impinging at centrally on the lower edge of the active area. As will be shown later in the Section IV, with this geometry, 6 γ- and 5 α-diffraction rings could be *partially* acquired, *i.e.*, the azimuthal range was ~ ± 100 deg for the lowest order reflections but decreased to ~ ± 30 deg for the highest ones. Before the actual measurements, the detector alignment was verified with a Si-powder specimen (NIST SRM 640f).

The X-ray diffraction data were analyzed with two main methods. In the first method, phase volume fractions were determined from diffractograms obtained by direct integration over the acquired azimuthal range,[31] *i.e.*, neglecting the effect of external loading on the ring shape. Here, the standard methodology[32] was followed; the integrated intensities of selected γ- and α-peaks in the diffractograms were normalized with the
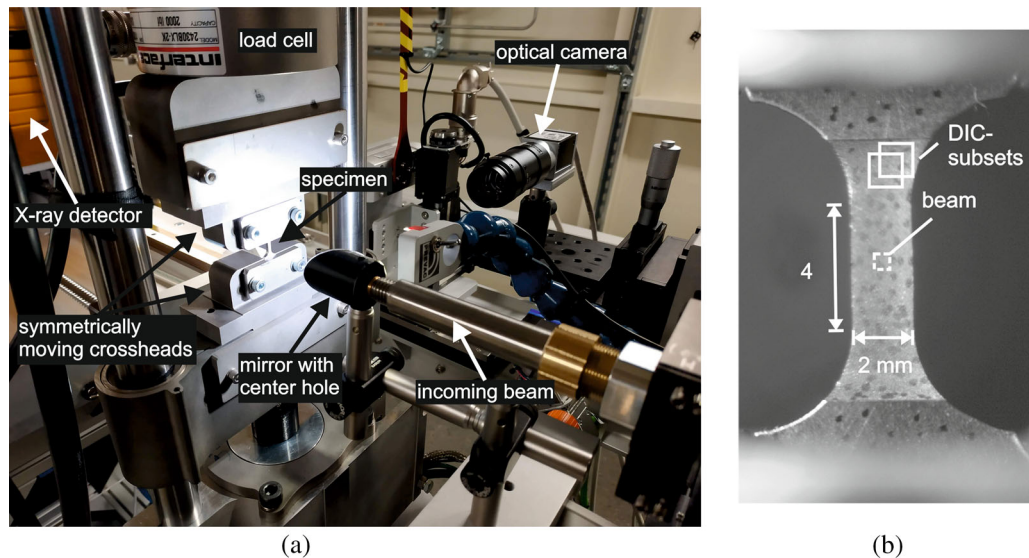
Fig. 2—Photos of (*a*) the test setup in the experimental hutch with main components highlighted, and (*b*) specimen as viewed by the optical camera *via* the mirror. The rectangles in (b) illustrate the X-ray beam size as well as the subset and step sizes used in the DIC analysis (Color figure online).

theoretical intensities (so-called *R*-values) and then compared with each other to obtain the phase volume fractions. In the analysis presented in this paper, the possible existence of the intermediate hexagonal ε-martensite phase was neglected due to its generally low volume fraction (according to Reference 9, the volume fraction remains less than 5 pct even in a fully austenitic steel). The second method involved the analysis of the diffraction ring shapes by fitting of Eq. [5] to the data, which provides data on the lattice strains. In this paper, linear least squares fitting was used for the detector pixel coordinates transformed into the $(1/\sin\theta, \cos^2\phi)$-space so that the pixel intensities were used as weight data for the fitting algorithm.

Uniaxial tensile loading on the specimen was carried out using a custom-made (Psylotech Inc., USA) loading device with two actuators moving at opposite directions, which kept the center of the specimen stationary during the test. The loading device was placed on remotely adjustable hexapod so that in the tests the incoming X-ray beam could be targeted at the center of the specimen. The loading device measured the axial load and the displacement of the two actuators.

The third main instrumentation of the setup comprised an optical camera (BASLER acA1300-75gc with a NAVITAR F2.8/50 mm objective) and a mirror placed upstream of the specimen at an angle of 45 deg. The mirror had a central hole through which the X-ray beam passed, whereas illumination needed for the optical imaging was provided with LED lights mounted on flexible arms. With this setup, full field image data of the front surface of the specimen could be collected (Figure 2(b)) and used in digital image correlation (DIC)-based deformation analysis carried out using LaVision DaVis 10 software. Thus, the specimen deformation could be accurately measured without the need to attach mechanical devices to the specimen, such as an

Table I. Main Digital Image Correlation Parameters

Sensor and Digitization	560×900 Pixels, 8 Bit
Camera Noise (Percent of Range)	0.7 pct
Image Scale Factor (pixel/mm)	61.8
Subset Size (pixel)	63
Step Size (pixel)	20
Axial Strain Resolution	0.00133 pct

extensometer, which could interfere with the X-ray diffraction measurement. The main parameters for the DIC analysis are shown in Table I. For the correlation algorithm to work, a stochastic pattern was manually made on the specimen surface by using a marker pen. A relatively coarse pattern was used instead of a fine (sprayed) pattern to avoid any interference with the X-ray beam. Even though the successful use of a sprayed pattern alongside synchrotron X-rays was reported recently by Abu-Farha,[33] in the current study, a coarse pattern was selected to maximize the success rate of the experiments within the available beamtime. In the subsequent analysis with other measurement data, the full field DIC data were reduced to scalar values with the use of a virtual extensometer placed on the parallel section of the specimen. The use of a virtual extensometer and a relatively large subset size facilitated good strain resolution despite the coarse speckle pattern. These data were then used alongside with the load data to calculate the classical engineering and true values of stress and strain in uniaxial loading. The true values were calculated up to the point of load maximum by assuming volume constancy; values beyond that, *i.e.*, during necking of the specimen, were omitted from the analysis.

The experiments were carried out at the strain rates of 10^{-3}, 0.1, and 1 s^{-1} with respective durations of ~ 500, ~ 5, and 0.5 seconds. Some trial measurements were

carried out at even higher loading rate, *i.e.*, 10 s^{-1} with test duration of ~ 0.05 seconds. The data sampling frequency of the loading device was 5, …, 5000 Hz depending on the strain rate. The diffraction patterns were collected at 10 Hz (exposure time 0.099 seconds, readout time 0.001 seconds) for the lowest strain rate and at the detector maximum of 250 Hz (exposure time 0.003 seconds, readout time 0.001 seconds) for the other strain rates. The respective values for the optical camera were 10 and 50 Hz (device maximum).

Synchronization of the various instruments was carried out in the following manner: in the beginning of each experiment, the specimen was preloaded to an axial load of 100 MPa in order to remove any free motion within the mechanical setup. Then the recording of the X-ray and optical data was started simultaneously using the same Transistor-Transistor Logic (TTL) trigger signal. After this the mechanical loading device was started by the operator. At this point, the loading device sent a TTL pulse, which was guided *via* auxiliary waveform generator to the X-ray data collection system, where it was saved as a data channel alongside with the time-stamped diffraction data frames. The rising edge of the TTL pulse thus provided a common reference time point for all the data channels with an accuracy relative to the X-ray detector frame rate (*i.e.*, 0.1 seconds in low rate tests and 0.004 seconds in high rate tests). Fine tuning of the synchronization at high loading rates was carried out in the post-test analysis of the results by comparing the time-histories of the mechanical load and the elastic strains deduced from the diffraction ring shape analysis and adding a constant time offset between the two data sources, if needed.

The test specimens discussed in this paper were manufactured from sheets of low-alloy multiphase steel designated as TR700 (the same material batch was recently studied in References 34, and 35 under the designation "TRIP 700") and a metastable austenitic stainless steel EN 1.4318-2B (the same batch was studied in Reference 2 under the designation "Batch A"). The specimens were prepared by laser-cutting and elec-tro-discharge machining (EDM) from the sheets. In order to establish high enough diffraction ring intensity, after preliminary trials, the original thickness (~ 2 mm) of the specimen gauge section was reduced to 0.5 mm *via* EDM (off-sided cut so that one of the original surfaces remained intact). The transmission of 0.354 Å X-rays through this thickness is approximately 13 pct (estimation based on data for pure Fe available at Reference 36). The test materials represent two different kinds of metastable austenite containing steels: the low-alloy steel contains primarily BCC or near-BCC-phases and a minor fraction (in the order of a few percent) of metastable FCC austenite phase, which, given suitable conditions, transforms into near-BCC martensite during loading. In contrast, the metastable austenitic stainless steel is nearly fully austenitic in the as-received state, but can undergo almost 100 pct transformation into martensite during deformation. For both alloys, the phase transformation is strongly strain rate and temperature dependent.[2,34,35]

In order to verify that the material behavior is not affected by the energy (heat) input from the X-ray beam, heat transfer analysis was carried out using the finite element method (steady-state heat transfer analysis in Abaqus Standard 3DEXPERIENCE R2017x). The energy from the beam was modeled by a 5 mW volume flux (estimated based on the beam energy and a 87 pct absorption) at the center of the specimen, while the material parameters were taken from a previous study.[2] The results of the numerical analysis indicated that the increase of specimen temperature due to the beam is negligible, *i.e.*, less than one degree. This conclusion was supported by experiments carried out at the beamline, in which a K-type thermocouple was placed directly into the incoming beam; also in this case, the increase in temperature was less than 1 deg. However, it should be noted that strictly speaking this conclusion holds only for the cases studied here, other materials might heat up differently depending on their X-ray absorption and thermal properties.

IV. RESULTS AND DISCUSSION

In the following, the main features of the experiments are presented and discussed starting from the quality of the diffraction data at different strain rates (time scales). Then ring shape analysis and temporal synchronization of the experiments are discussed. Finally, novel data for an experiment involving an upward strain rate jump are presented.

A. *Diffraction Data Measured at Different Strain Rates*

Figure 3 shows diffraction data acquired in a test of the metastable austenitic stainless steel at the strain rate of 1 s^{-1} (test duration ~ 0.7 seconds, 250 Hz diffraction data resulting in ~ 100 diffraction frames collected during specimen deformation). Figures 3(a) and (b) show the raw detector frames at zero strain and at the true strain of 0.33, respectively, whereas Figure 3(c) shows the data of (b) in polar coordinates (*i.e.*, diffraction angle 2θ – azimuthal angle ϕ). Several points are evident; firstly, as already noted, a wide azimuthal range ($\pm$ 90 deg) of the rings is acquired only for the lowest reflections, and secondly, due to the construction of the detector, the frames are gridded with zero-value pixels in between. Thus the diffraction rings are only partially recorded, which should be taken into account especially when strong texture develops during plastic deformation.

Closer examination of Figure 3(c) shows that the diffraction lines are not exactly straight and horizontal but they show curvature as predicted in the theory section. This will be discussed later in detail in conjunc-tion with the lattice strain analysis. However, for the volume fraction analysis, it suffices that azimuthal integration is carried out directly on the raw data as long as no overlapping rings are used in the analysis. Figure 3(d) presents the diffractograms for the raw frames shown in (a) and (b) (the evolution of the diffractograms during the test is presented in the
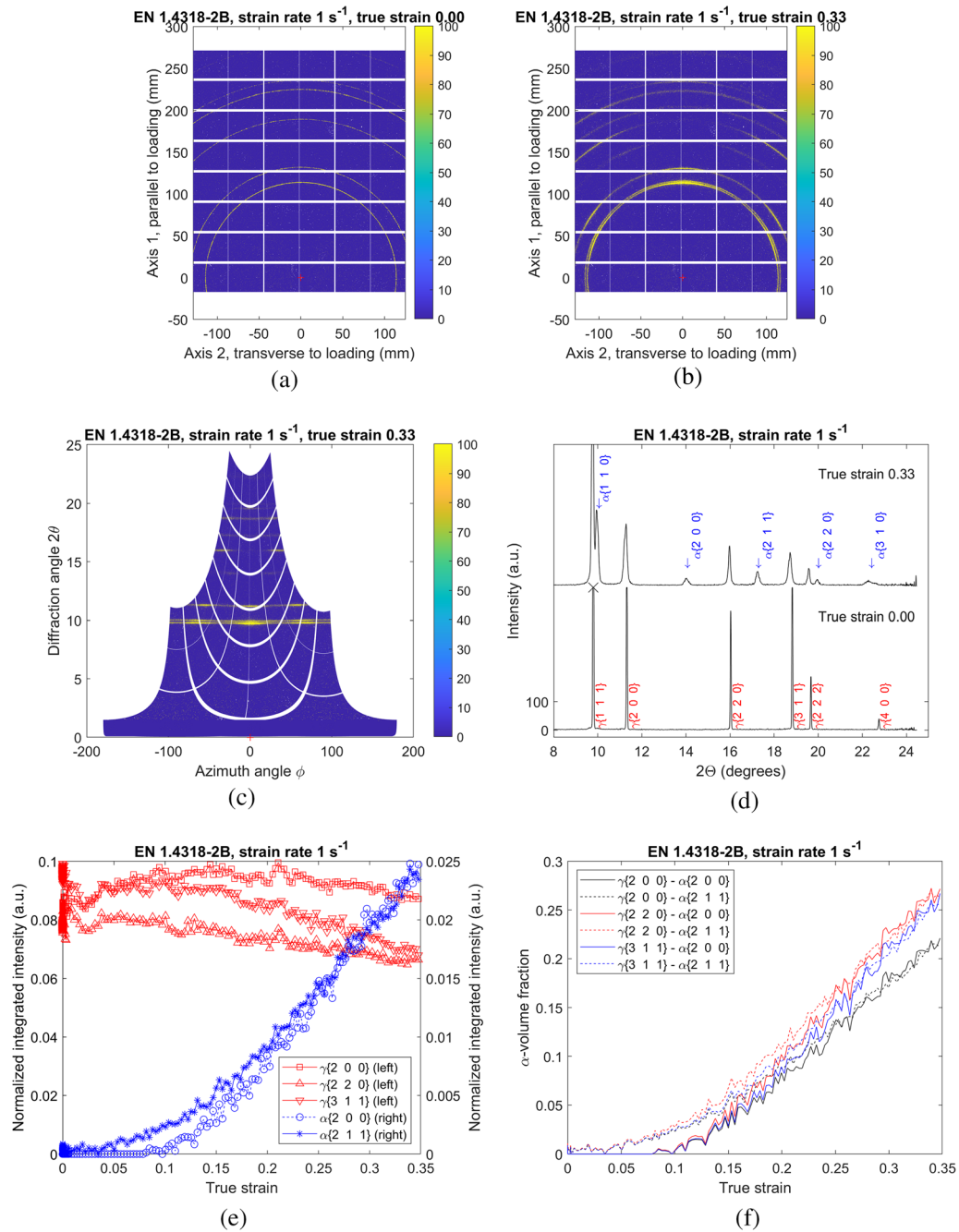
Fig. 3—Example of the diffraction data obtained during a test of the metastable austenitic stainless steel EN 1.4318-2B at the strain rate of 1 s^{-1}: (*a*) and (*b*) raw detector data at true strains of 0 and 0.33, respectively, (*c*) the data shown in (b) converted into polar coordinates (2θ, ϕ), (*d*) azimuth-integrated intensities (diffractograms) of the raw data, and (*e*) evolution of the integrated intensities of selected γ- and α-peaks (normalized with the respective *R*-values), and (*f*) the α-volume fraction for the different γ/α-peak combinations obtained by direct comparison of the intensities in (e). In (a) through (c), the intensity data have been truncated, and in (d), the $\gamma\{111\}$ peak has been cropped to improve clarity.

Appendix Figure A1)). As demonstrated by the data in Figure 3(d), the peak-to-background ratio is very good throughout the measured angular range and remains good despite the plastic deformation and strain-induced phase transformation from FCC austenite (γ) to near-BCC martensite (α). Similar conclusions could be made also for tests at low strain rates, where up to 90 pct of the austenite transforms into martensite. Figure 3(e) depicts the normalized intensities of three austenite and

two martensite peaks, whereas Figure 3(f) presents the calculated martensite volume fraction for the altogether six austenite/martensite-peak combinations. It should be noted that the high intensity $\gamma\{111\}$, and $\alpha\{110\}$ peaks were not analyzed because they overlap in the test material. As can be seen, relatively consistent data are obtained from the different rings despite the fact that, as seen in the detector data (Figures 3(a) through (c)), strong texture (*i.e.*, intensity variation as a function of

the azimuthal angle) develops in the austenite rings. Furthermore, the individual peak intensities might be somewhat affected by the formation of a small amount of hexagonal ε-martensite (according to Reference 17, ε-martensite rings appear close to the γ{220}, and γ{311} as well as α{211} rings). The development of a more detailed phase volume fraction analysis, which is able to account for these effects automatically for hundreds of diffraction frames, is, however, left for future studies.

Figure 4 demonstrates the quality of the diffraction data measured at different strain rates. For this comparison, data from tests of the low-alloy TR700 steel were selected, since the phase volume fractions evolve less with plastic deformation than in the case of the metastable austenitic stainless steel,[2,34,35] thus facilitating a more straightforward comparison. As can be seen, the very good signal-to-noise ratio is maintained throughout the studied strain rate range which covers nearly static experiments lasting several minutes and, on the other end of the range, experiments in the so-called intermediate strain rate region lasting some tens of milliseconds. In fact, in the experimental campaign reported here, the limiting factors at the highest strain rate of $10 \ s^{-1}$ were the maximum frame rate of the available optical camera (50 Hz) and the structural vibrations of the mechanical frame which interfered with the load measurement.

B. Correlation Between Lattice Strain and External Loading

Figures 5 and 6 show an example of the diffraction ring shape and mechanical data analysis of a test for the metastable austenitic stainless steel carried out at the strain rate of $1 \ s^{-1}$. As explained in the theory section, external load affects the diffraction rings so that they become ellipses with their minor axis aligned along the loading direction and major axis along the transverse direction. This is illustrated by Figure 5(a) for an austenite {200} ring shown in polar coordinates (2θ, ϕ), whereas Figure 5(b) shows the same data after

transforming the azimuthal axis from ϕ to $\cos^2 \phi$ values. As can be seen, the theoretical predictions hold well, and the diffraction ring center line can be described by a fit of the linear function given by Eq. [5].

Figure 6(a) illustrates the temporal synchronization of the various data sources: the external load measured by the mechanical loading device, the specimen gauge section strain based on the DIC analysis of the optical images as well as the lattice strain determined by analyzing the γ{200} ring. As explained in the Section III, the synchronization between the different data sources was achieved by taking the trigger signal sent by the loading device as a common starting point and then fine tuning between the load frame data and the diffraction data. The optical data were assumed to be synchronized with the diffraction data. As can be seen in Figure 6(a), very good temporal synchronization is achieved both in terms of the beginning of external loading (at 0.32 seconds in Figure 6(a)) and in terms of the specimen failure (at 0.98 seconds in Figure 6(a)).

Figure 6(b) demonstrates the benefits of using the optical non-contact strain measurement; the use of nominal strain based on the crosshead displacement would lead to notable overestimation of specimen strain due to load frame compliance and specimen deformation taking place outside the gauge section. In contrast, with the optical extensometer in the DIC analysis, the average specimen gauge section strain can be accurately determined throughout the test. A natural development step forward here is the incorporation of a finer speckle pattern, which increases the spatial resolution of the DIC analysis and facilitates the measurement of strain localization phenomena alongside with the synchrotron X-ray characterization of strain-induced phase transformations, similarly to the low rate experiments reported in Reference 33.

Figure 6(c) presents lattice elastic strains deduced from different austenite reflections (γ{111}, γ{200}, and γ{311}) with respect to the externally applied stress measured by the loading device. The presented data were collected within ~ 0.1 seconds after the start of the
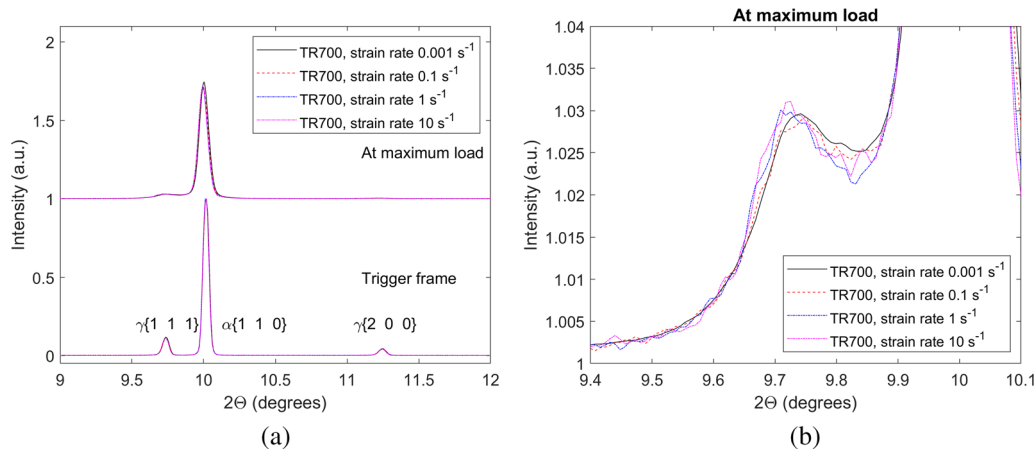

Fig. 4—(a) Part of the diffractograms obtained in tests at different strain rates for the low-alloy steel TR700 immediately prior to loading and at the point of maximum load, and (b) zoom-in on the data near the γ{111} peak at maximum load. The diffractograms have been displaced along the intensity axis for clarity and the intensity data have been scaled so that the α{110} peak height is unity at the trigger frame.
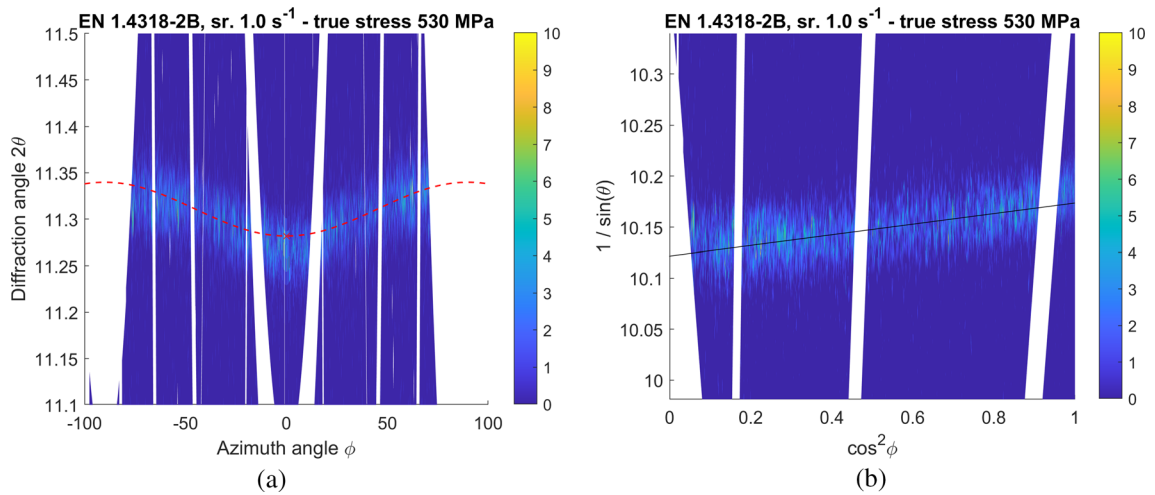
Fig. 5—Example of the diffraction ring shape analysis: (a) an austenite {200} ring in the $(2\theta - \phi)$-coordinates, and (b) the same data converted into the $(1/\sin\theta, \cos^2\phi)$-coordinates. The results of the least squares fitting of Eq. [5] are superimposed on the figures.

loading. The uncertainty of the lattice strain (depicted in Figure 6(c) by the error bars) was estimated by modifying the approach suggested by Schuren and Miller.[37] They used the data for a powder calibration specimen to fit an uncertainty model, which incorporated minimum resolvable peak shift on the detector and the effect of varying peak intensity. In the current study, the availability of data on statically preloaded tensile test specimen (recorded prior to the tensile test) allowed direct analysis of the noise level for the actual diffraction rings used in the analysis. For the test shown in Figure 6, the uncertainty analysis resulted in minimum resolvable ring shifts of 1.8, 3.3, and 5.2 μm for the $\gamma\{111\}$, $\gamma\{200\}$, and $\gamma\{311\}$ rings (the values are for 95 pct confidence). Thus, the respective strain uncertainties are below $\pm 0.5 \times 10^{-4}$ for the rings used in the analysis (with the assumption that the ring intensity does not change markedly, which applies for the data shown in Figure 6(c)). It should be noted that the estimated uncertainty is in the same order of magnitude as in the previous study.[37]

Superimposed in Figure 6(c) are the respective diffraction elastic moduli (261, 155, and 193 GPa) reported by Clausen et al.[38] for a stable austenitic stainless steel. As can be seen, at small stress levels (below 350 MPa), the measured lattice strains increase linearly with the external stress and the slopes agree fairly well with the literature values. However, at higher stress levels, the strain response of the reflections starts to deviate from linearity. This was reported also by Clausen et al.,[38] who noted that the deviation from linearity starts for most reflections already before macroscopic yielding. They related the nonlinearity to heterogeneously distributed plastic deformation between different grain orientations, which affects the load partitioning and hence the elastic strains. In the current work, a further influencing factor is the martensitic phase transformation which leads to re-partitioning of the load as well. A

more detailed analysis of these effects is reserved for further studies.

Based on the discussion presented in this and in the previous chapters, it is concluded that the applied methodology is suitable for *in-situ* diffraction analysis during plastic deformation at strain rates up to 1 s^{-1}. A high number of diffraction frames are collected and very good temporal synchronization is obtained so that detailed analysis of the phase transformation kinetics during various stages of the loading can be made. An example of the application of the methodology is given in the following section.

C. *Application of the Methodology to a Strain Rate Jump Test*

In the following, data for a so-called strain rate jump test are presented and discussed. In this test, the strain rate is suddenly changed during plastic deformation by changing the crosshead velocity and the resulting material response (change in flow stress, strain hardening rate, *etc.*) is analyzed. Typically the strain rate jump tests are used to study thermally activated deformation mechanisms, such as dislocation slip, because they enable one to study the effect of strain rate on flow stress on a quasi-constant microstructure and temperature (these parameters are assumed to change very little as the strain rate is suddenly changed). In an earlier study,[39] it was found that strain rate jump tests can also be effectively used to study the kinetics of strain-induced martensitic phase transformations by separating the effects of material temperature increase (due to adiabatic heating) and the direct effects of strain rate (such as on the formation rate of shear bands, which act as nucleation sites for the α'-martensite[40]). The main finding of this approach, which was later verified,[41,42] is that the strain hardening rate of a readily transforming metastable austenitic stainless steel decreases
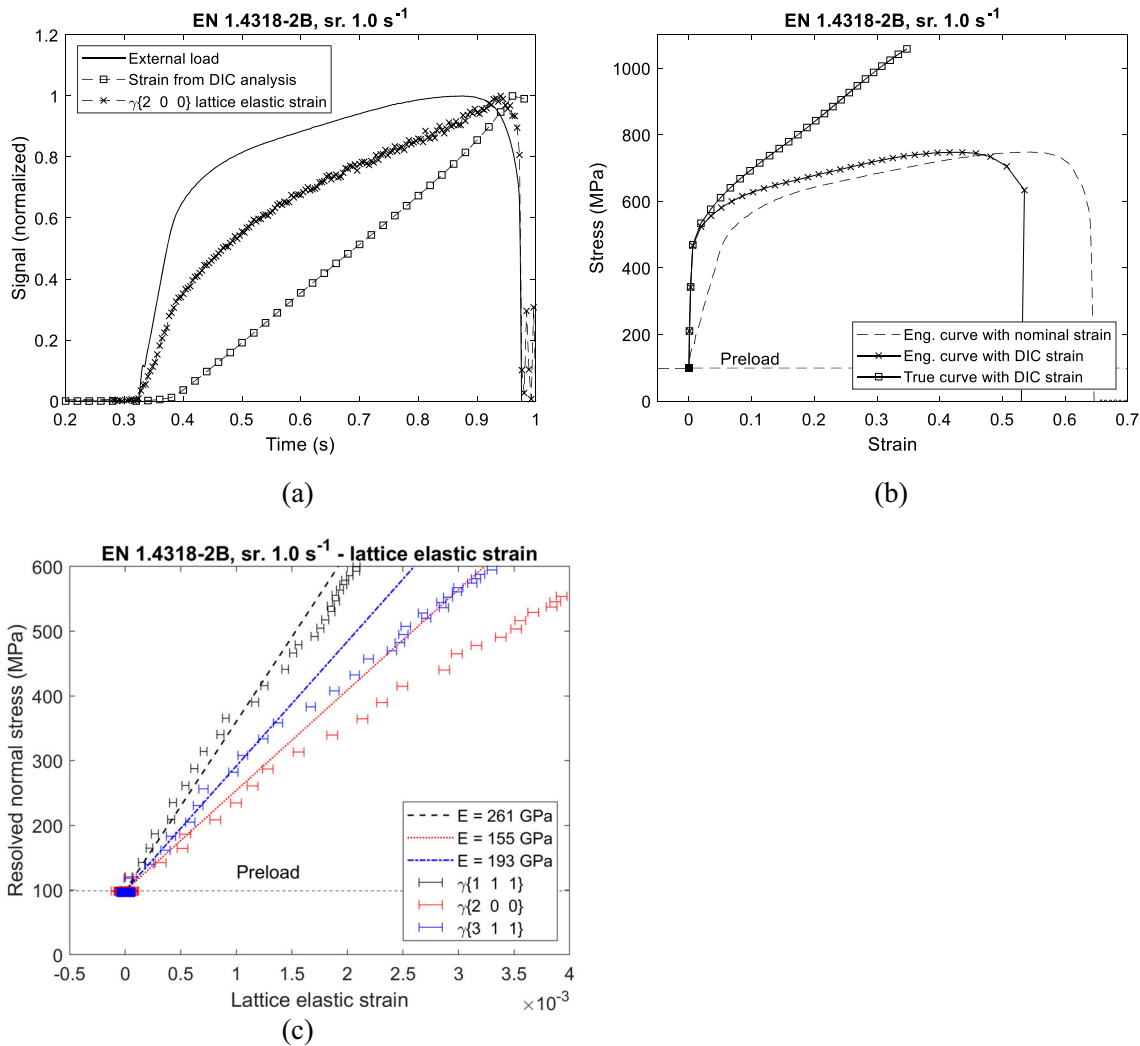
Fig. 6—Example of an experiment carried out for the metastable austenitic stainless steel EN 1.4318-2B at the strain rate of 1 s⁻¹: (a) illustration of the synchronization of the various data sources (signals normalized to 0, …, 1), (b) stress–strain curves obtained by combining the mechanical and optical data, and (c) evolution of austenite lattice strains with respect to the external stress acting on the lattice planes, data from the early part of the test. The error bars in (c) represent 95 pct confidence limits determined based on the resolution of the ring shape analysis during static external loading.

immediately after the increase in strain rate even though the increase in temperature following the jump is modest, as shown in Reference 42 for the same alloy as in the current study. This finding implies an immediate reduction in the phase transformation rate after the jump, which cannot be fully explained with the commonly accepted theory of bulk adiabatic heating causing the suppression of the strain-induced martensitic transformation. Thus, the topic deserves further attention. Unfortunately, until now the means to directly study the martensitic phase transformation during a strain rate jump have been very limited with data available only from some interrupted tests.[39] This gave strong motivation to apply the *in-situ* diffraction measurements on a strain rate jump test.

Figure 7 presents data from a strain rate jump test of the metastable austenitic stainless steel EN 1.4318-2B. The strain rate jump was done at the true strain of 0.12 from the strain rate of 0.001 to 1 s⁻¹. Since the two

strain rates and the associated time scales differ from each other by three orders of magnitude and hence require different data acquisition parameters, a special technique was implemented in the execution of the test. The mechanical loading device was programmed to run uninterrupted through two sequences, the low and high rate portion of the test, with predetermined length and appropriate data collection frequencies. Furthermore, at the beginning of both sequences, the device sent a trigger signal to the X-ray data collection system and optical camera similarly to the monotonic tests. For the X-ray diffraction and optical measurements, the data collection had to be interrupted and the devices reset manually with new acquisition parameters. This was carried out just before the strain rate jump, while the deformation of the specimen continued uninterrupted. In this manner, high-frequency X-ray and optical data collection started already before the jump took place and the trigger signal coming from the mechanical
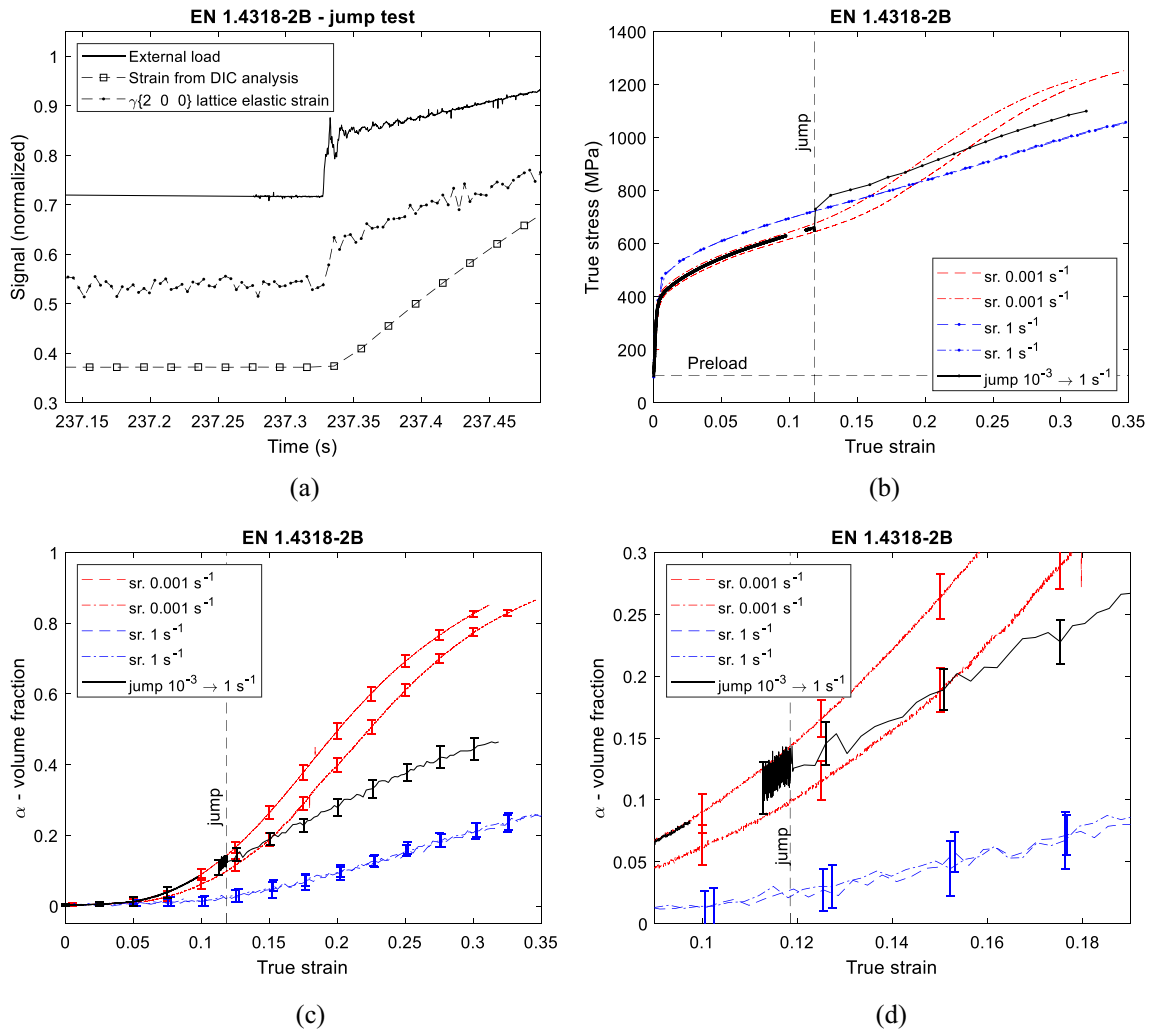
Fig. 7—Example of the strain rate jump methodology used to study the phase transformation kinetics of the metastable austenitic stainless steel EN 1.4318-2B: (*a*) synchronization of the data at the moment of the strain rate jump, (*b*) true stress–strain curves of monotonic tests at strain rates of 0.001, and 1 s^{-1} and the corresponding strain rate jump test, (*c*) evolution of the martensite volume fraction in the tests shown in (a), and (*d*) zoom-in on (c) at the moment of the strain rate jump. For clarity, the error bars, which represent the standard deviation between the six γ/α-peak combinations shown in Fig. 3, are drawn only for selected data points in the graphs.

loading device was recorded simultaneously. As is evidenced by Figure 7(a), the trigger signals and the analysis of the lattice strains allowed very good synchronization of the data despite the interruption in the data collection. Furthermore, due to the low strain rate of the first part of the test and well-coordinated work of the operators, the amount of data lost during resetting is acceptable, *i.e.*, corresponding to ~ 1 pct of deformation.

Figures 7(b) through (d) compare the data collected from the strain rate jump test with data from monotonic tests with corresponding strain rates. The measured stress strain response and the strain rate sensitivity of flow stress shown in Figure 7(b) agree with the data from earlier studies.[39,41,42] The strain hardening rate (slope of the stress strain curve) decreases after the jump close to the same level as in the monotonic test at 1 s^{-1}, whereas continued deformation at the low rate (0.001 s^{-1}) leads to a notable increase in the strain hardening rate. Similar conclusions apply to the evolution of the martensite volume fraction shown by Figures 7(c) and (d). Even though there is some noise in the data prior to the jump (resulting from the high data collection rate), the evidence is clear: as the strain rate is suddenly increased from 0.001 to 1 s^{-1}, the phase transformation rate (slope of the curves in Figures 7(c) and (d)) decreases to a low level, which is only slightly higher than in the corresponding monotonic test at 1 s^{-1}. This finding is in accordance with the earlier study[39] carried out with *ex-situ* methods.

V. CONCLUSIONS

In this work, the methodology and experimental techniques related to *in-situ* characterization of the kinetics of martensitic phase transformations taking place during plastic deformation are described and discussed. The experimental campaign involved mechanical loading of metastable austenite containing steel specimens at a wide strain rate range of 0.001 to $1\ s^{-1}$ with simultaneous synchrotron radiation-based X-ray diffraction measurements, which were supplemented by optical measurements of specimen deformation. As demonstrated by the examples in this paper, excellent synchronization between the different instruments (mechanical loading device, the diffraction measurement setup and the optical camera) could be obtained even at high loading rates. This facilitates detailed studies on the effects of strain rate on mechanically induced phase transformations in steels and other alloys involving metastable phases, as exemplified by the novel results of a strain rate jump experiment carried out on a metastable austenitic stainless steel.

CONFLICT OF INTEREST

On behalf of all authors, the corresponding author states that there is no conflict of interest.

APPENDIX

Figure A1 presents the evolution of the azimuth-integrated diffraction data (diffractogram) as a function of strain in the test shown by Figure 3 of the main text.
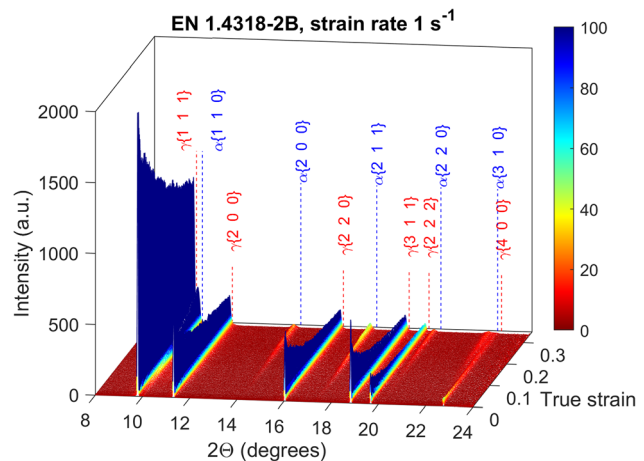

Fig. A1—Illustration of the evolution of the azimuth-integrated diffraction data as a function of strain in the test shown by Fig. 3 in the main text. The color scaling has been set so that intensity values above 100 are shown by constant color (blue) (Color figure online).

REFERENCES

1. C. Enloe, V. Savic, W. Poling, L. Hector, and R. Alturk: *SAE Int. J. Adv. Curr. Pract. Mobil.*, 2019, vol. 1, pp. 1046–55.
2. M. Isakov, M. May, S. Hiermaier, and V.-T. Kuokkala: *Mater. Des.*, 2016, vol. 106, pp. 258–72.
3. M. Thrun, C. Finfrock, A. Clarke, and K. Clarke: *Front. Mater.*, 2021, vol. 7, p. 615361.
4. M. Radu, J. Valy, A.F. Gourgues, F. Le Strat, and A. Pineau: *Scripta Mater.*, 2005, vol. 52, pp. 525–30.
5. D. Maréchal, C.W. Sinclair, P. Dufour, P.J. Jacques, and J.-D. Mithieux: *Metall. Mater. Trans. A*, 2012, vol. 43A, pp. 4601–9.
6. K. Yvell, T.M. Grehk, P. Hedström, A. Borgenstam, and G. Engberg: *Mater. Charact.*, 2018, vol. 135, pp. 228–37.
7. L. Pun, G. Corrêa Soares, M. Isakov, and M. Hokka: *Mater. Sci. Eng. A*, 2022, vol. 831, p. 142218.
8. M. Lindroos, M. Isakov, and A. Laukkanen: *Int. J. Solids Struct.*, 2022, vol. 236–237, p. 111322.
9. P. Hedström, U. Lienert, J. Almer, and M. Odén: *Scripta Mater.*, 2007, vol. 56, pp. 213–16.
10. E. Jimenez-Melero, N.H. van Dijk, L. Zhao, J. Sietsma, J.P. Wright, and S. van der Zwaag: *Mater. Sci. Eng. A*, 2011, vol. 528, pp. 6407–16.
11. R. Blondé, E. Jimenez-Melero, L. Zhao, J.P. Wright, E. Brück, S. van der Zwaag, and N.H. van Dijk: *Acta Mater.*, 2012, vol. 60, pp. 565–77.
12. K. Yan, K.-D. Liss, I.B. Timokhina, and E.V. Pereloma: *Mater. Sci. Eng. A*, 2016, vol. 662, pp. 185–97.
13. P. Eftekharimilani, R.M. Huizenga, B. Kim, A. Bernasconi, and M.J.M. Hermans: *Metall. Mater. Trans. A*, 2018, vol. 49A, pp. 78–87.
14. Y. Tian, S. Lin, J.Y.P. Ko, U. Lienert, A. Borgenstam, and P. Hedström: *Mater. Sci. Eng. A*, 2018, vol. 734, pp. 281–90.
15. J. Hidalgo, R.M. Huizenga, K.O. Findley, and M.J. Santofimia: *Mater. Sci. Eng. A*, 2019, vol. 745, pp. 185–94.
16. X. Zhang, C. Xu, Y. Chen, W.-Y. Chen, J.-S. Park, P. Kenesei, J. Almer, J. Burns, Y. Wu, and M. Li: *Acta Mater.*, 2020, vol. 200, pp. 315–27.
17. P. Barriobero-Vila, R. Jerez-Mesa, A. Guitar, O. Gavalda-Diaz, J.A. Travieso-Rodríguez, A. Stark, N. Schell, J. Llumà, G. Fargas, A. Mateo, and J.J. Roa: *Materialia*, 2021, vol. 20, p. 101251.
18. C.B. Finfrock, B. Ellyson, S.R.J. Likith, D. Smith, C.J. Rietema, A.I. Saville, M.M. Thrun, C.G. Becker, A.L. Araujo, E.J. Pavlina, J. Hu, J.-S. Park, A.J. Clarke, and K.D. Clarke: *Acta Mater.*, 2022, vol. 237, p. 118126.
19. R. Lin Peng, G. Chai, N. Jia, Y.D. Wang, and S. Johansson: *Fatigue Fract. Eng. Mater. Struct.*, 2008, vol. 31, pp. 892–901.
20. S. Harjo, N. Tsuchida, J. Abe, and W. Gong: *Sci. Rep.*, 2017, vol. 7, p. 15149.
21. R. Voothalurua, V. Bedekar, Q. Xie, A.D. Stoica, R.S. Hyde, and K. An: *Mater. Sci. Eng. A*, 2018, vol. 711, pp. 579–87.
22. M. Hudspeth, T. Sun, N. Parab, Z. Guo, K. Fezzaa, S. Luo, and W. Chen: *J. Synchrotron Radiat.*, 2015, vol. 22, pp. 49–58.
23. C.S. Meredith, Z. Herl, and M.L. Young: *Dynamic Behavior of Materials, Volume 1. Conference Proceedings of the Society for Experimental Mechanics Series*, Springer, Cham, 2019.
24. D. Zhang, C. Yu, M. Wang, S. Chen, C. Huang, D. Sun, S. Yue, Y. Tao, and B. Zhang: *Rev. Sci. Instrum.*, 2022, vol. 93, p. 033902.
25. C.B. Finfrock, B. Ellyson, C.G. Becker, J. Copley, K. Fezzaa, N. Parab, T. Sun, C. Kirk, N. Kedir, W. Chen, A. Clarke, and K. Clarke: *Metall. Mater. Trans. A*, 2022, vol. 53A, pp. 3528–35.
26. B. Ellyson, K. Fezzaa, T. Sun, N. Parab, A. Saville, C. Finfrock, C.J. Rietema, D. Smith, J. Copley, C. Johnson, C.G. Becker, J. Klemm-Toole, C. Kirk, N. Kedir, J. Gao, W. Chen, R. Banerjee, K.D. Clarke, and A.J. Clarke: *Mater. Sci. Eng. A*, 2022, vol. 857, p. 143716.
27. J.A. Copley, F.G. Coury, B. Ellyson, J. Klemm-Toole, J. Frishkoff, C. Finfrock, Z. Fisher, N. Kedir, C. Kirk, W. Chen, N. Parab, T. Sun, K. Fezzaa, K.D. Clarke, and A.J. Clarke: *Metall. Mater. Trans. A*, 2022, vol. 53A, pp. 1821–30.
28. M. Fitzka, H. Rennhofer, D. Catoor, M. Reiterer, H. Lichtenegger, S. Checchia, M. di Michiel, D. Irrasch, T.A. Gruenewald, and H. Mayer: *Exp. Mech.*, 2020, vol. 60, pp. 317–28.
29. P.S. Prevéy: *Metals Handbook*, vol. 10, American Society for Metals, Metals Park, 1986, pp. 380–92.
30. M.L. Young, J.D. Almer, M.R. Daymond, D.R. Haeffner, and D.C. Dunand: *Acta Mater.*, 2007, vol. 55, pp. 1999–2011.
31. A.B. Jensen, T.E.K. Christensen, C. Weninger, and H. Birkedal: *J. Synchrotron Radiat.*, 2022, vol. 29, pp. 1420–8.
32. ASTM Standard E975-13: *Standard Practice for X-ray Determination of Retained Austenite in Steel with Near Random Crystallographic Orientation*, ASTM International, West Conshohocken, 2013.
33. F. Abu-Farha, X. Hu, X. Sun, Y. Ren, L.G. Hector Jr., G. Thomas, and T.W. Brown: *Metall. Mater. Trans. A*, 2018, vol. 49A, pp. 2583–96.
34. M. Hokka, V.-T. Kuokkala, and S. Curtze: *Steel Res. Int.*, 2009, vol. 80, pp. 137–45.
35. S. Curtze, V.-T. Kuokkala, M. Hokka, and P. Peura: *Mater. Sci. Eng. A*, 2009, vol. 507, pp. 124–31.
36. J.H. Hubbel, S.M. Seltzer: *X-ray Mass Attenuation Coefficients*, NIST Standard Reference Database 126. https://doi.org/10.18434/T4D01F.
37. J.C. Schuren and M.P. Miller: *J. Strain Anal. Eng. Des.*, 2011, vol. 46, pp. 663–81.
38. B. Clausen, T. Lorentzen, M.A.M. Bourke, and M.R. Daymond: *Mater. Sci. Eng. A*, 1999, vol. 259, pp. 17–24.
39. M. Isakov, S. Hiermaier, and V.-T. Kuokkala: *Metall. Mater. Trans. A*, 2015, vol. 46A, pp. 2352–5.
40. J. Talonen, P. Nenonen, G. Pape, and H. Hänninen: *Metall. Mater. Trans. A*, 2005, vol. 36A, pp. 421–32.
41. S. Sunil and R. Kapoor: *Metall. Mater. Trans. A*, 2020, vol. 51A, pp. 5667–76.
42. N.I. Vázquez-Fernández, M. Isakov, and M. Hokka: *J. Dyn. Behav. Mater.*, 2022, vol. 8, pp. 316–21.